

# New approach for measuring migration properties of point defects in amorphous oxides

Ekaterina Dikarov, Roman Shklyar, and Aharon Blank\*

Schulich Faculty of Chemistry, Technion – Israel Institute of Technology, Haifa 32000, Israel

Received 27 February 2014, revised 11 May 2014, accepted 12 May 2014

Published online 5 June 2014

**Keywords** amorphous materials, defect migration, electron spin resonance, oxides, point defects

\* Corresponding author: e-mail ab359@tx.technion.ac.il, Phone: +972 4 829 3679, Fax: +972 4 829 5948

Amorphous oxides are key ingredients in electronic and optical devices. Such oxides include a variety of point defects that greatly affect their electrical and optical properties. Many of these defects are paramagnetic, and as such, the best tool to identify and characterize their structure is electron spin resonance (ESR). However, due to its limited sensitivity and spatial resolution, ESR cannot provide information about the defects' migration properties, which are of crucial importance for device fabrication. Ultra-high-resolution imaging modalities

such as TEM, as well as theoretical calculations, are severely limited in amorphous media, resulting in a wide gap of knowledge in this field. Here, a novel method of ESR microimaging is applied for the first time to examine unique samples that are prepared using electron-beam irradiation and have well-defined point defects patterns. This provides a capability to unambiguously identify the defects and at the same time track their migration with high spatial resolution, revealing new information about their properties.

© 2014 WILEY-VCH Verlag GmbH & Co. KGaA, Weinheim

**1 Introduction** Amorphous oxides are indispensable ingredients in modern semiconductor-based devices, serving mostly as insulators (e.g., SiO<sub>2</sub> or HfO<sub>2</sub>) [1]. As such, they are crucial to the performance of the device and any defect in their structure can have dramatic consequences on the latter's electrical properties [2, 3]. The amorphous nature of such oxides makes them inaccessible to conventional microscopy tools, especially when seeking information about point defects in the bulk material in a nondestructive manner; as a result, there is a wide gap of knowledge in this field [4]. The information sought includes defect properties such as: (1) microscopic–atomic structure; (2) charge; (3) diffusion properties; (4) activation energy; and (5) possible interaction energy between defects. These important properties remain mostly inaccessible to high-resolution imaging and related experimental techniques. Many point defects are paramagnetic and as such can be analyzed by ESR spectroscopy [5, 6]. If the solid is optically opaque and/or the defect is non-fluorescent, ESR is the only methodology that can unambiguously identify and address such point defects. However, due to its limited sensitivity and spatial resolution, conventional ESR works well only with large homogenous samples. Thus, apart from providing unequaled information about the defect's atomic structure [5], ESR cannot actually help with the other four

properties mentioned above (2)–(5). As a result, information about these properties remains largely unknown or is very controversial at best for many important types of point defects.

A good case in point is SiO<sub>2</sub>, which is obviously the most important oxide in the semiconductor industry. It is a well-known fact that point defects in SiO<sub>2</sub> play a crucial role in device performance [3]. For example, these defects can become electrically active and act as traps for charge carriers in systems based on SiO<sub>2</sub>/Si interfaces. This can lead to an uncontrolled change in the device's characteristics and to accelerated aging. One such common defect is known as the E'<sub>γ</sub> center, which is attributed to the dangling bond of the silicon near an oxygen vacancy that is connected to only three oxygen atoms in an sp<sup>3</sup> hybridization [6]. (A similar defect in crystalline SiO<sub>2</sub> is denoted as E'<sub>1</sub>, and will not be dealt with here.) The properties of this defect, originally identified and atomically characterized by ESR [7], are still largely unknown or debated almost 60 years after its discovery. For example, some literature data claim that it is positively charged [8, 9] with the hole positioned on the neighboring silicon atom, while other recent results argue that it is neutral [10, 11]. Its diffusion properties, migration energy, and interaction energy are largely unknown due to the abovementioned experimental difficulties (with the

exception of our preliminary work on this subject [12]). In view of the lack of experimental approaches, another possibility is to resort to theoretical treatments. However, here also there are various models and conflicting possibilities regarding the structural and diffusion properties of  $E'$  centers in amorphous  $\text{SiO}_2$  [13–15]. This spread of theoretical results is possibly due to the amorphous nature of the material, which makes theoretical calculation extremely difficult. (For example, even for “simple” amorphous  $\text{SiO}_2$  without defects, properties such as bond length distributions are controversial [16].)

In this work we provide a new methodology for determining properties (2)–(5) listed above for point defects in oxides, based on high spatial resolution ESR microimaging. ESR is used both as a *spectroscopic* tool to unambiguously determine the identity of the defects and also as an *imaging* tool to observe their diffusion and migration properties following heat treatments. We apply this methodology to the case of an  $E'_\gamma$  center point defect in amorphous  $\text{SiO}_2$ , and to its “associated” defect,  $E'_\beta$  [6, 17]. The method is based on generating a well-defined rectangular feature of point defects with steep borders using high energy electron-beam irradiation, and measuring the development of the defects’ spatial distribution following various heating cycles during constant time periods. The latter is achieved by obtaining high-resolution ( $\sim 1.6 \mu\text{m}$ ) ESR microimages of the point defects using state-of-the-art methodologies recently developed by our group.

**2 Experimental details** Samples of amorphous  $\text{SiO}_2$  with  $E'$  point defects in a fixed rectangular pattern of  $600 \mu\text{m} \times 300 \mu\text{m}$  (see Fig. 1) were prepared by irradiating  $150 \mu\text{m}$  thick  $\text{SiO}_2$  slips (material GE 124 from Specialty Glass Products, USA). These slips have very low impurity concentrations ( $\text{OH} < 5 \text{ ppm}$ ,  $\text{Al} = 14 \text{ ppm}$ ,  $\text{Ti} = 1.1 \text{ ppm}$ ;  $\text{Na} = 0.7 \text{ ppm}$  and other metals less than  $1 \text{ ppm}$ ). The slips were first covered with a 30-nm chrome layer (to prevent surface charging) and then irradiated by electron irradiation using the JEOL JSM 6400 e-beam lithography system. The irradiation energy was set at 30 keV and the beam’s aperture size was  $120 \mu\text{m}$ , which resulted in a beam diameter of  $\sim 10 \mu\text{m}$  on the sample. The sample received irradiation charge density of  $(1/4)(\text{C}/\text{cm}^2)$  (dose of  $\sim 1.7 \times 10^9 \text{ Gy}$ ).

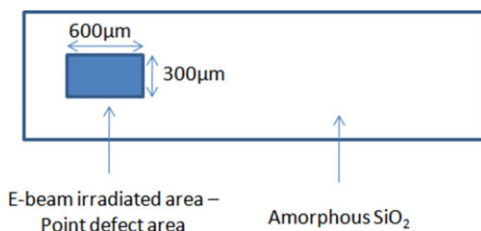


**Figure 1** Drawing of the rectangular feature created by e-beam irradiation of an amorphous  $\text{SiO}_2$  slide. The slide is  $150 \mu\text{m}$  thick and the point defects are found to be at the depth of up to  $\sim 16 \mu\text{m}$ .

After irradiation, the chrome layer was removed using CR-7 chromium etchant.

Continuous-wave ESR measurements were carried out at room temperature using a Bruker EMX X-band system at 9.248 GHz with microwave power of 0.63 mW, modulation amplitude of 1 G, and averaging time of 1.16–4.66 h. The pulsed electron spin resonance (ESR) microimaging system operating at the Q-band frequency range ( $\sim 34 \text{ GHz}$ ) that was employed in this work is described in details in Ref. [18]. Briefly, it consists of a home-made pulsed ESR spectrometer and powerful magnetic field gradient drivers that enable the 3D spatial encoding of the ESR signal. The heart of the system is a unique high sensitivity imaging probe that comprises a  $\sim 1.1 \text{ mm}$  dielectric ring resonator (made from  $\text{TiO}_2$  single crystal) and a set of miniature gradient coils. For the present measurements carried out at room temperature, this system can provide spin sensitivity of  $\sim 2.7 \times 10^6$  spins for 1 h of acquisition. This high spin sensitivity, combined with the powerful magnetic gradient drivers, enables an ESR image resolution down to  $\sim 440 \text{ nm}$  in some paramagnetic samples. In the present set of experiments we made use of a simple Hahn echo imaging sequence (see Fig. 2), with a pulse duration of 50 ns and 90-ns pulse separation,  $t = 650 \text{ ns}$ , and repetition rate of 8000 Hz. The total acquisition time for each image was 17 h. To guarantee a stable static field throughout this long acquisition period, we made use of a field-frequency-lock mechanism. It periodically measures the ESR spectrum without any signal and corrects for small static field changes by changing a small bias field on one of the coils in the imaging probe [18].

**3 Results** Following the sample preparation, the first stage in our experiments was to characterize the identity of the defects in the irradiated  $\text{SiO}_2$  samples. This was carried out by conventional CW ESR spectroscopy; typical results

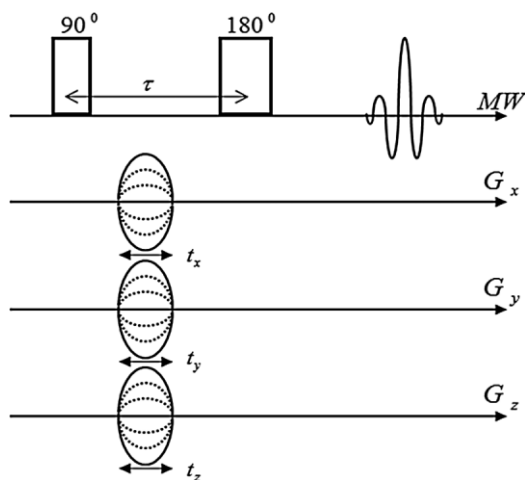


**Figure 2** Pulsed sequence diagram used for obtaining 2D and 3D ESR images. In the case of 2D imaging, only the  $G_x$  and  $G_y$  phase gradients are applied. For 3D imaging, all the phase gradients are used.

are provided in Fig. 3a. The spectrum was fitted using EasySpin software [19]. The results showed that the spectrum is composed of two major contributions, one from an  $E'_\gamma$  defect and the other from an  $E'_\beta$  defect, both of which have been well-characterized by ESR [6] ( $E'_\gamma$  has  $g$ -factors of  $g_x, g_y, g_z = [2.0018, 2.0006, 2.0003]$ , and  $E'_\beta$ :  $[2.0018, 2.0004, 2.0004]$ ). The theoretical best fit to the experimental spectrum was obtained with an  $E'_\gamma/E'_\beta$  ratio of 0.25 using the above-mentioned  $g$ -factors that are taken from Ref. [6]. The currently known information about the microscopic structure of  $E'_\gamma$ , based on ESR data, was mentioned above. As for the  $E'_\beta$  defect, it also originates from oxygen vacancy and has an unpaired electron spin on the Si dangling bond similar to that of  $E'_\gamma$ , but with a hydrogen atom attached to its adjacent Si atom. Subsequent heating cycles over 3 and 6 h at temperatures of 300, 400, 450, and 500 °C (using four different samples), showed a significant decrease in total ESR signal intensity down to 0.5, 0.3, 0.13, and 0.12 of the original signal strength, as a function of heating temperatures, respectively. This annealing phenomenon of point defects is well known in the literature [20, 21]. A typical spectrum following the heating

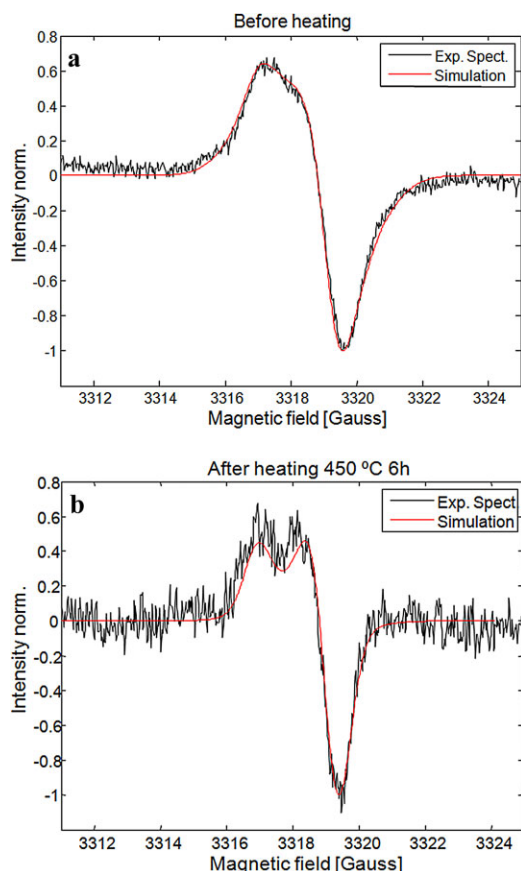


**Figure 3** Continuous-wave ESR spectra of the irradiated  $\text{SiO}_2$  samples before (a) and after a 6-h heating cycle at 450 °C (b). The black line shows the measured spectra and the red line shows the simulated results using the known  $g$ -value parameters for  $E'_\gamma$  and  $E'_\beta$ .

cycles at 450 °C is shown in Fig. 3b. The change in the spectral shape can be accounted for by modifying the  $E'_\gamma/E'_\beta$  ratio in the simulation from its initial value of 0.25, up to 5, after the heating cycle. Similar analysis of the spectra after the 300, 400, and 500 °C heat cycles provides  $E'_\gamma/E'_\beta$  ratios of 0.5, 1, and 10, respectively. This rapid annealing of the  $E'_\beta$  defects, as compared to  $E'_\gamma$ , is known in the literature [17].

Following and in parallel to defect identification and characterization by CW ESR, the same samples were examined using high-resolution pulsed ESR microimaging. Several 3D and 2D images were acquired before and after each heating cycle. Typical experimental 3D images are shown in Fig. 4. They reveal that the depth of penetration of the e-beam radiation is  $\sim 16 \mu\text{m}$ . Typical 2D images acquired before and after the heating cycle of 400 °C are shown in Fig. 5. They were acquired with an anisotropic resolution of  $\sim 1.6$  and  $27 \mu\text{m}$  along the  $Y$  and  $X$  axes, respectively. The analysis of these images makes it possible to learn about the migration behavior of the defects. Each image was slightly rotated so that its  $X$  and  $Y$  axes coincided exactly with the long and short directions of the rectangular irradiated feature, respectively. Following that, a one-dimensional projection along the  $X$ -axis was generated, showing more clearly the changes in defect spatial distribution along the  $Y$ -axis due to migration processes. Figure 6 shows the 1D projection results before and after the heating cycles, at four different temperatures (after proper alignment of the projections to enable an easy comparison). The variations in the projections' full width at half maximum due to the heating

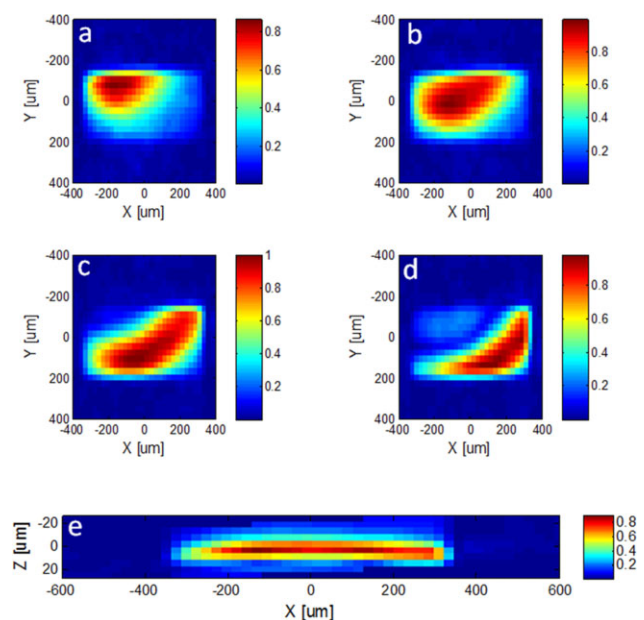


**Figure 4** (a–d) Several  $XY$  slices taken out of a 3D image obtained by pulsed ESR imaging of the electron-irradiated  $\text{SiO}_2$  sample. The resolution along the  $X$  and  $Y$  axes is of 24 and  $30 \mu\text{m}$ , respectively. (e)  $ZX$  slice taken out of a 3D image. The resolution along the  $Z$ -axis is  $5 \mu\text{m}$ . This cross-section shows the penetration of the electrons into the sample, which is  $\sim 16 \mu\text{m}$ .

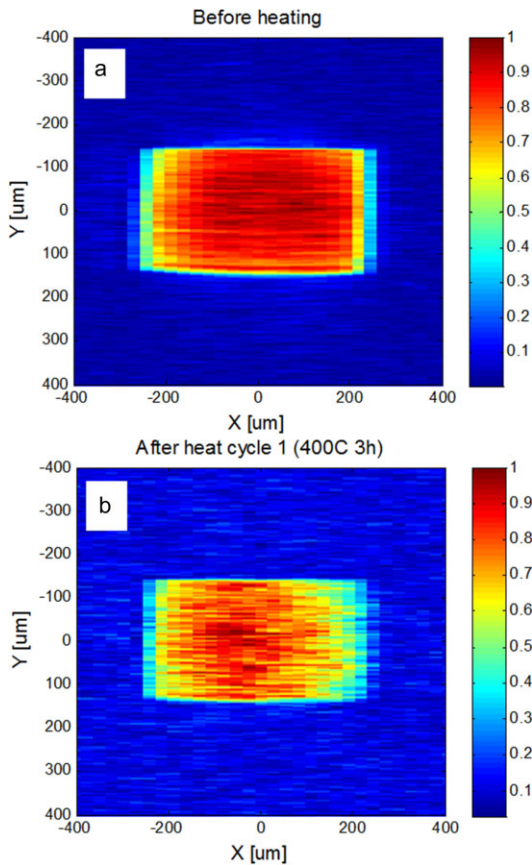


**Figure 5** Pulsed ESR 2D images of the irradiated SiO<sub>2</sub> sample before (a) and after (b) heating cycle at 400 °C for 3 h.

cycles were evaluated and are summarized in Table 1. It is obvious from the figures that after the first heating cycle the width of the projection decreases considerably, while after the second heating cycle the change is much smaller. The higher the heating cycle temperature, the stronger the reduction of the projection's width.

**4 Discussion** From a qualitative standpoint, these observations can be explained by assuming that the defects migrate under some attractive potential that pushes them inwards. A similar phenomenon was observed using photoluminescence in point defects in bulk SiC [17]. Such attraction potential can be due to strain effects (see below) but not to electric charges, which would push the defects outwards. These strain effects decrease significantly in the second heating cycle, probably because the defects' distribution has reached some local energy minimum after their initial migration. Thus, our first conclusion out of these measurements is that the defects we observe using ESR *are not charged*. This is also supported by the clear rectangular pattern observed in the ESR image, which precludes the possibility of charged defects that would greatly distort the e-beam trajectory. Comparing it with Fig. 7, it shows the same images collected with samples under charging

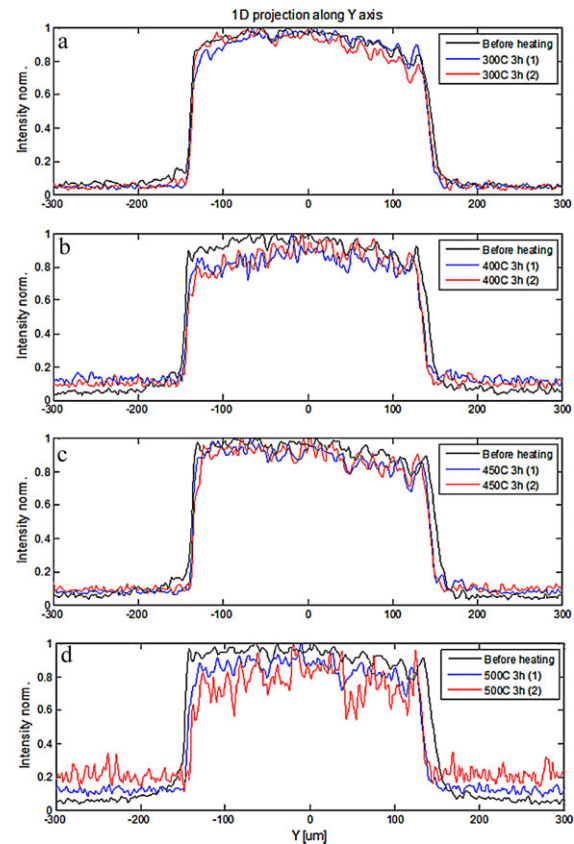


**Figure 6** One-dimensional projection results for four different SiO<sub>2</sub> samples as obtained from the 2D ESR images, before the heating cycles (black line) and after the first (blue line) and second (red line) heating cycles. The intensity of the projections was normalized to facilitate an easy comparison between them even though the signal drops significantly after each heating cycle due to annealing.

conditions and demonstrates the existence of significant pattern broadening and smearing effects due to charge.

An alternative explanation of our observations can be that the image is contracted due to contraction of the entire SiO<sub>2</sub> wafer. However, this was ruled out by measuring similar samples that had two features that exhibited independent contraction (Figs. 8 and 9). Furthermore, AFM measurements also show very small changes in sample morphology due to irradiation (densification of ~40 nm), meaning that the wafer dimensions almost do not change (Fig. 10). The sample linear densification fraction in this vertical dimension is therefore 40 nm/16 μm = ~0.0025 (based on the 16 μm vertical thickness of the irradiated volume – see Fig. 4). This value is ~2.7 times smaller than the densification fraction predicted for the type of material used here for the 1.7 × 10<sup>9</sup> Gy irradiation dose [22]. This is quite a good agreement, taking into consideration that we irradiated only small part of the sample so that densification is expected to be strongly eliminated by forces from the surrounding nonirradiated areas. This means that for the irradiated 300 μm wide spot along the Y-axis, the expected

**Table 1** Changes of the half-width profile of the defect feature following various heating cycles and the associated diffusion coefficient and attraction force constants, calculated on the basis of the numerical solution of Eq. (1).

sample no.	temperature of the heat cycle (°C)	half-width change after heating cycle #1 ( $\mu\text{m}$ ) ( $\pm 1.6$ )	half-width change after heating cycle #2 ( $\mu\text{m}$ ) ( $\pm 1.6$ )	$D$ ( $\text{m}^2 \text{s}^{-1}$ ) heating cycle 1	$k_f$ ( $\text{J m}^3$ )
1	300	−3.5	−0.1	$1.3 \times 10^{-15}$	$5 \times 10^{-45}$
2	400	−9.9	−0.35	$4.6 \times 10^{-15}$	$5 \times 10^{-45}$
3	450	−16.9	−0.8	$9.5 \times 10^{-15}$	$5 \times 10^{-45}$
4	500	−19.5	−5.7	$1.2 \times 10^{-14}$	$5 \times 10^{-45}$

densification is less than  $1 \mu\text{m}$ , which is a far smaller change than the one observed after heating. Thus, to conclude this point, the sample's density does increase after irradiation, as we observed using AFM. However, this densification is quite small and it seems unlikely that the sample would continue to densify after heating, especially by a factor larger by more than one order of magnitude.

Further to the charge properties (#2 in the list above) that were deduced based on qualitative considerations, a quantitative analysis of the imaging results can provide valuable information about the migration properties of the defects (properties (3)–(5) listed above). To that end, we use the diffusion equation with some attractive force between the defects. This can be mathematically formulated within the framework of the Fokker–Planck equation [23]:

$$J(\mathbf{r}) = -D \frac{\partial C(\mathbf{r})}{\partial \mathbf{r}} + DC(\mathbf{r}) \cdot \frac{F(\mathbf{r})}{k_B T}, \quad (1)$$

where  $J(\mathbf{r})$  is the flux of defects,  $D$  is the diffusion coefficient,  $C(\mathbf{r})$  is the concentration of defects,  $\mathbf{r}$  is the position vector,

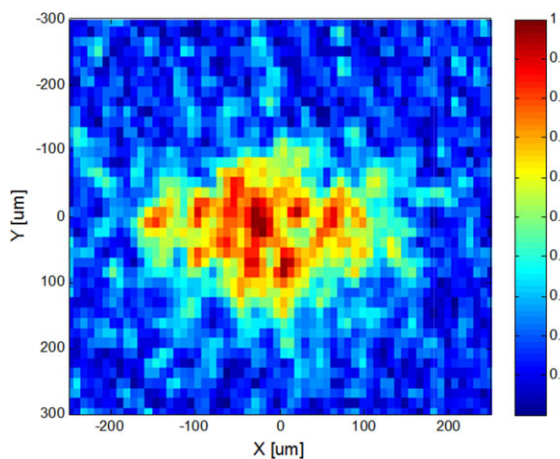


**Figure 7** Typical ESR microimage of a  $\text{SiO}_2$  sample irradiated with an e-beam to create a pattern with dimensions of  $300 \times 150 \mu\text{m}^2$ , but without applying a Cr mask to eliminate charging effects. Similar images were obtained for  $\text{SiO}_2$  wafers with a thickness of  $400 \mu\text{m}$  from the same manufacturer that provided our prime  $150 \mu\text{m}$  samples, which had a different elemental composition (OH concentration of  $\sim 100$  ppm) leading to the creation of charged paramagnetic defects even when applying a Cr mask.

$k_B$  is the Boltzmann constant, and  $T$  is the temperature. The solution of Eq. (1) for the 1D case can be obtained using numerical calculations starting from the initial measured projection and then propagating the defects' concentration through time, subjected to diffusion and the attractive force. The concentration of the defects inside the rectangular feature is practically constant before the heating cycles (which were found to be at a saturation level of

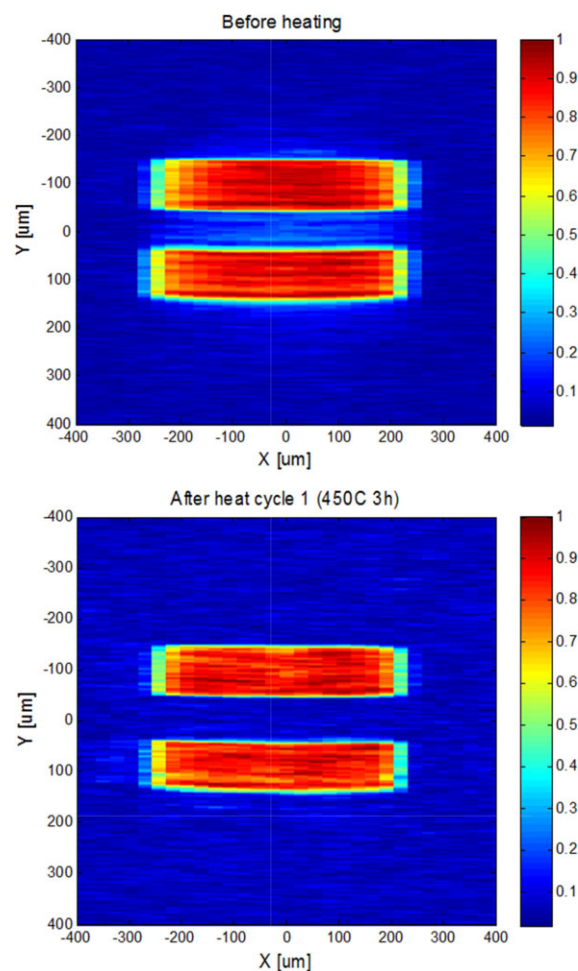


**Figure 8** Two-dimensional pulsed ESR images of electron-irradiated  $\text{SiO}_2$  before (upper image) and after (lower image) heat treatment at  $450^\circ\text{C}$  for 3 h. The sample has two rectangular irradiated features with dimensions of  $600 \times 100 \mu\text{m}^2$  that are parallel to each other, with a vertical separation of  $100 \mu\text{m}$ .

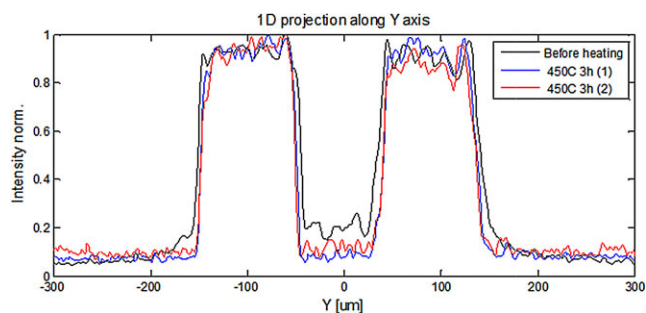


**Figure 9** One-dimensional projection results for the sample appearing in Fig. 8 as obtained from the 2D ESR images, before the heating cycles (black line) and after the first (blue line) and second (red line) heating cycles. The intensity of the projections was normalized to facilitate an easy comparison between them even though the signal drops significantly after each heating cycle due to annealing.

$\sim 2 \times 10^{17}$  spins  $\text{cm}^{-3}$ ). Therefore, the numerical solution has only two fitting parameters –  $D$  and  $F$ . Both can provide valuable information about some of the microscopic properties of the defects. Here we assume that the force  $F(\mathbf{r})$  is the result of an elastic interaction between the defects due to strain generated in the solid [24]. Elastic interaction models have various possibilities for the parametric dependence of the force between individual point defects and their separating distance, ranging from  $1/r^4$  to  $1/r^7$  [25]. The case of point defects in amorphous  $\text{SiO}_2$  can have various theoretical options for this dependence, so we chose the force  $F_{ij}$  between two defects to be  $F_{ij} = k_F |\mathbf{r}_i - \mathbf{r}_j|^{-4}$ ; this

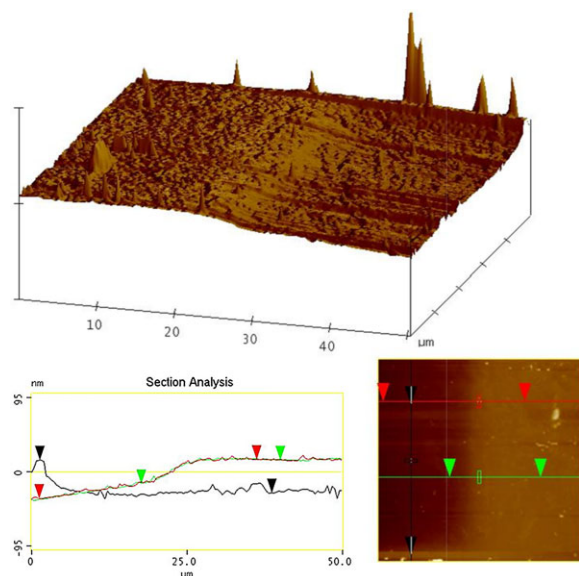


**Figure 10** AFM data as measured for a typical irradiated  $\text{SiO}_2$  wafer showing minimal changes in sample morphology. Vertical distances of  $\sim 30.3$  nm (green),  $\sim 50.4$  nm (red), and  $\sim 42.1$  nm (black) were measured near the edge of the irradiated area. The change occurs over a distance of  $\sim 5$ – $10$   $\mu\text{m}$ .

choice was found to be the one that recreates best the migration phenomenon we observe through the model of Eq. (1). (Here,  $k_F$  is a force constant and  $|\mathbf{r}_i - \mathbf{r}_j|$  is the distance between defects in bins  $i$  and  $j$  of the projection.) In the 1D projection case, each defect “sees” the attractive force acting upon it from a certain volume of defects. Thus, a defect in bin  $m$  of the projection would experience a force of  $F(\mathbf{r}) \approx (k_F C_j / |\mathbf{r}_m - \mathbf{r}_n|^2) |\mathbf{r}_m - \mathbf{r}_n|^{-2} \times (4\pi/8)$  coming from some of the defects in bin  $n$  (see Fig. 11). This simple force model is plugged into the numerical solutions of Eq. (1), which are compared to the experimental data, resulting in the fitting parameters appearing in Table 1 for  $k_F$  and  $D$  as a function of heating temperature.

The diffusion coefficients obtained as a function of temperature can be fitted to a simple Arrhenius model resulting in  $D = 9.5 \times 10^{-12} e^{-0.438/k_B T}$  [ $\text{m}^2 \text{s}^{-1}$ ], where the activation energy is in electronvolt (eV) units. (Due to the limited temperature range of our measurements, the margins of error for the pre-exponential factor and the activation energy are  $\pm 15\%$  and  $\pm 3\%$ , respectively.) This result indicates that the point defect migration most probably does not involve oxygen bond breaking, which would mean a much higher activation energy (about 4.5 eV is needed to break the Si–O bond). The low activation energy assumption is supported also by the rapid rate of annealing at relatively low temperatures. A possible explanation for the relatively low activation energy is that the defects migrate by moving through pre-existing oxygen vacancies in the amorphous structure and just open up a weak Si–Si bond. An additional explanation could be that the diffusion/migration process is assisted by other impurities in the material, based on previous studies that show large differences in the annealing temperature of  $E'$  defects for different impurity concentrations [21]. Alternatively, the migration can be mediated by an iterative interconversion between different possible

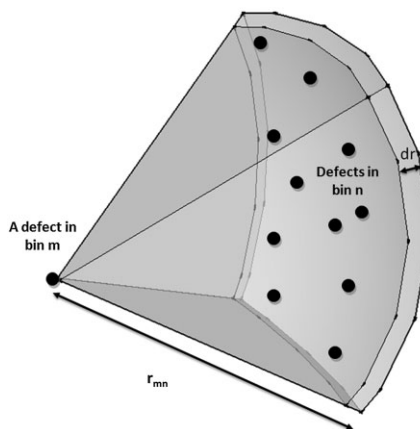


**Figure 11** Simplified model that was used to estimate the number of defects in bin  $n$  of the projection that attract a single defect in bin  $m$ . It shows that only some of the defects in bin  $n$  that are located in a  $\sim 18$  sphere shell with thickness  $dr$  attract the single defect in bin  $m$ . In the model we took  $dr$  to be equal to the bin size ( $Y$ -axis resolution of 1.6  $\mu\text{m}$ ).

atomic configurations, as has been theorized for  $E'_1$  defects in  $\alpha$ -quartz [26, 27], which gives possible activation energies of 0.4 and 0.59 eV (but for positively charged defects).

The force constant that was found by fitting the numerical solution of Eq. (1) to the experimental observations is  $k_F \sim 5 \times 10^{-45} \text{ J m}^3 = 3.1 \times 10^{-26} \text{ eV m}^3$ . This can be compared to fundamental strain theory [24] that describes interaction energy between point defects to be of the order of  $E_{\text{int}} \sim -K(a_0/r)^3$ , where  $E_{\text{int}}$  is expressed in eV,  $a_0$  is the lattice constant, and  $K$  is of the order of 1–10 (dimensionless). In the case of amorphous  $\text{SiO}_2$ , an approximate lattice constant of 5 Å can be used, leading to  $E_{\text{int}} \sim -K \times (1.25 \times 10^{-28}/r^3) \text{ eV m}^3$ , or to a force constant of  $k_{F(\text{theory})} \sim 1.25 \times 10^{-28} \times K \times 3 \text{ eV m}^3$  (after applying a derivative to the interaction energy to obtain the force). This results in  $K \sim 82.6$ , which is rather high but still in the relevant order of magnitude. The defect's concentration could be somewhat higher than we estimated through our measurements, which would lead to a corresponding decrease in the fitted  $K_F$  and  $K$ .

**5 Conclusions** In conclusion, it was shown that the combination of spectroscopic ESR with high-resolution ESR imaging capabilities and well-defined samples can provide a new and powerful tool for the quantitative analysis of point defects in amorphous oxides. The qualitative interpretation of our observations makes it clear that the defects we observe are not charged, while quantitative analysis through simplified diffusion and strain theory provides the first direct observation of properties such as migration activation energy, diffusion coefficient, and magnitude of interaction energy between two defects. Certainly, there is much more to be done, both in terms of improving the experimental methodology and providing a more solid theoretical treatment of our observations. These combined efforts can close a wide gap of knowledge that currently exists for the properties of point defects in amorphous oxides, which are of significant importance to modern semiconductor and optical applications.

**Acknowledgements** This work was partially supported by grant # G-1032-18.14/2009 from the German-Israeli Foundation (GIF), grant #213/09 from the Israel Science Foundation (ISF), grants #201665 and #309649 from the European Research Council (ERC), and by the Russell Berrie Nanotechnology Institute at the Technion.

## References

- [1] J. S. Park, W. J. Maeng, H. S. Kim, and J. S. Park, *Thin Solid Films* **520**, 1679 (2012).
- [2] H. L. Tuller and S. R. Bishop, *Annu. Rev. Mater. Res.* **41**, 369 (2011).
- [3] D. M. Fleetwood, S. T. Pantelides, and R. D. Schrimpf, *Defects in Microelectronic Materials and Devices* (CRC Press, Boca Raton, Fla., 2008).
- [4] M. A. Stoneham, J. L. Gavartin, and A. L. Shluger, *J. Phys.: Condens. Matter* **17**, S2027 (2005).
- [5] S. Johann-Martin and O. Harald, *Point Defects in Semiconductors and Insulators* (Springer, Berlin, Heidelberg, 2003).
- [6] G. Pacchioni, L. Skuja, and D. L. Griscom, *Defects in  $\text{SiO}_2$  and Related Dielectrics: Science and Technology* (Kluwer Academic Publishers, Dordrecht, Netherlands, Boston, MA, 2000).
- [7] R. A. Weeks, *J. Appl. Phys.* **27**, 1376 (1956).
- [8] W. L. Warren, J. Kanicki, F. C. Rong, and E. H. Poindexter, *J. Electrochem. Soc.* **139**, 880 (1992).
- [9] A. Kimmel, P. Sushko, A. Shluger, and G. Bersuker, *ECS Trans.* **19**, 3 (2009).
- [10] V. V. Afanas'ev and A. Stesmans, *J. Phys.: Condens. Matter* **12**, 2285 (2000).
- [11] L. Skuja, M. Hirano, H. Hosono, and K. Kajihara, *Phys. Status Solidi C* **2**, 15 (2005).
- [12] E. Suhovoy, V. Mishra, M. Shklyar, L. Shtirberg, and A. Blank, *Europhys. Lett.* **90**, 26009 (2010).
- [13] S. T. Pantelides, Z. Y. Lu, C. Nicklaw, T. Bakos, S. N. Rashkeev, D. M. Fleetwood, and R. D. Schrimpf, *J. Non-Cryst. Solids* **354**, 217 (2008).
- [14] G. Roma, Y. Limoge, and S. Baroni, *Phys. Rev. Lett.* **86**, 4564 (2001).
- [15] P. V. Sushko, S. Mukhopadhyay, A. S. Mysovsky, V. B. Sulimov, A. Taga, and A. L. Shluger, *J. Phys.: Condens. Matter* **17**, S2115 (2005).
- [16] K. Minjung, K. H. Khoo, and J. R. Chelikowsky, *Phys. Rev. B* **86**, 054104 (2012).
- [17] J. W. Steeds, W. Sullivan, A. Wotherspoon, and J. M. Hayes, *J. Phys.: Condens. Matter* **21**, 364219 (2009).
- [18] L. Shtirberg, Y. Twig, E. Dikarov, R. Halevy, M. Levit, and A. Blank, *Rev. Sci. Instrum.* **82**, 043708 (2011).
- [19] E. Tatsukawa, Y. Gonda, M. Kamitakahara, M. Matsuura, M. Ushijima, Y. Shibata, I. Yonezawa, M. Fujiwara, K. Ioku, and T. Ikeda, *J. Orthop. Res.* **32**, 189 (2014).
- [20] L. Nuccio, S. Agnello, and R. Boscaino, *J. Phys.: Condens. Matter* **20**, 385215 (2008).
- [21] D. L. Griscom, *Nucl. Instrum. Methods Phys. Res. B* **1**, 481 (1984).
- [22] G. Buscarino, S. Agnello, F. M. Gelardi, and R. Boscaino, *J. Phys.: Condens. Matter* **22**, 255403 (2010).
- [23] P. Pichler, *Intrinsic Point Defects, Impurities, and Their Diffusion in Silicon* (Springer, Wien, New York, 2004).
- [24] J. D. Eshelby, *Solid State Phys.* **3**, 79 (1956).
- [25] R. W. Balluffi, *Introduction to Elasticity Theory for Crystal Defects* (Cambridge University Press, Cambridge, New York, 2012).
- [26] T. Laino, D. Donadio, and I. F. W. Kuo, *Phys. Rev. B* **76**, 195210 (2007).
- [27] J. Y. Song, L. R. Corrales, G. Kresse, and H. Jonsson, *Phys. Rev. B* **64**, 134102 (2001).